# Generation of Collimated Bright Gamma Rays with Controllable Angular Momentum Using Intense Laguerre-Gaussian Laser Pulses

L.B. Ju (鞠立宝),[1,2] C.T. Zhou (周沧涛),[1,3,4,*] T.W. Huang (黄太武),[1] K. Jiang (蒋轲),[5] C.N. Wu (伍超能),[5] T.Y. Long (龙天云),[4] L. Li (李玲),[4] H. Zhang (张华),[1] M.Y. Yu (郁明阳),[1] and S.C. Ruan (阮双琛)[1,3,†]

[1] *Center for Advanced Material Diagnostic Technology, College of Engineering Physics, Shenzhen Technology University, Shenzhen 518118, People's Republic of China*

[2] *Key Laboratory of Optoelectronic Devices and Systems of Ministry of Education and Guangdong Province, College of Physics and Optoelectronic Engineering, Shenzhen University, Shenzhen 518060, People's Republic of China*

[3] *College of Applied Technology, Shenzhen University, Shenzhen 518060, People's Republic of China*

[4] *Center for Applied Physics and Technology, HEDPS, and School of Physics, Peking University, Beijing 100871, China*

[5] *Graduate School, China Academy of Engineering Physics, Beijing 100088, People's Republic of China*

(Received 29 March 2019; revised manuscript received 25 June 2019; published 29 July 2019)

A scheme to produce mega-electron-volt- (MeV) level gamma rays with a high level of brilliance, a small divergence angle, and controllable angular momentum from Laguerre-Gaussian (LG) laser-pulse interactions with underdense plasma is proposed. Three-dimensional particle-in-cell simulations show that the gamma photon beam acquires angular momentum from the helically distributed relativistic electrons driven by the LG laser and the self-generated fields in the plasma bubble created by the laser. The divergence angle and the orbital angular momentum (OAM) of the gamma photons can be controlled by manipulating the laser parameters. It is found that a 1-MeV helical gamma-ray pulse with peak brightness $2.23 \times 10^{24}$ photons/s/mm$^2$/mrad$^2$/0.1% BW and angular momentum $7.1 \times 10^{-15}$ kg m$^2$/s, as well as a $< 10^{\circ}$ divergence angle, can be generated by a $2 \times 10^{22}$ W/cm$^2$ right-hand circularly polarized LG laser pulse. Such bright gamma rays with OAM offer an additional degree of freedom, which is relevant for understanding quantum-electrodynamics phenomena involving angular momentum, astrophysical phenomena, time-resolved probing of the nucleus, the generation of a vortical positron beam, etc.

DOI: 10.1103/PhysRevApplied.12.014054

## I. INTRODUCTION

Bright gamma-ray sources have a broad range of applications involving quantum-electrodynamic (QED) effects, probing the structure of the nucleus, ultrahigh-density matter radiography, high-flux positron generation, nuclear medical imaging, gamma-knife surgery, etc. [1–5]. Traditional accelerators for producing intense gamma rays are bulky and expensive [6]. In contrast, laser-driven tabletop accelerators are compact and of low cost. Gamma rays can be generated from bremsstrahlung of fast electrons interacting with high-$Z$ materials [7–9], nonlinear Thomson and Compton back-scattering [10–17], as well as nonlinear synchrotron radiation [18–26]. Recent experiments have shown that the peak brightness of over-15-MeV gamma rays from Thomson scattering can reach approximately $10^{20}$ photons/s/mm$^2$/mrad$^2$/0.1% BW [12]. Simulations have shown that gamma rays with a peak brightness of $10^{25}$ photons/s/mm$^2$/mrad$^2$/0.1% BW (at 10 MeV) can be obtained when relativistic electrons driven by a laser in a plasma channel collide with the same laser reflected by a solid wall [13]. However, such all-optical schemes can only be realized with laser intensities exceeding $10^{23}$ W/cm$^2$. Lasers with an intensity of about $10^{22}$ W/cm$^2$ are available at present [27] and $10^{23}$–$10^{24}$ W/cm$^2$ lasers are expected in a few years' time [28].

It is known that x rays can also carry orbital angular momentum (OAM) [29–32]. In particular, such beams with OAM are relevant to many applications, such as optical microscopy, micromanipulation, quantum information, magnetism, chirality, and astronomy. However, there are few ways to achieve OAM for gamma rays with much higher photon energies. Recently, it has been proposed that it is possible to obtain bright gamma rays with OAM by using an ultraintense Laguerre-Gaussian (LG) laser pulse interacting

*zcangtao@sztu.edu.cn
†scruan@sztu.edu.cn

 

with a thin solid target that produces the radiating electrons [33]. It is noted that in previous schemes, bright gamma rays usually have a $> 30^\circ$ divergence angle and $> 10^{23}$ W/cm$^2$ lasers are needed to obtain them [33–36]. So far, the generation of bright gamma rays with controllable OAM and a low divergence angle using the available lasers that are far below $10^{23}$ W/cm$^2$ has not been reported.

In this paper, we propose a scheme for electron acceleration by an intense short circularly polarized (CP) LG laser in underdense plasma for producing multi-mega-electron-volt bright gamma rays with controllable OAM and a small divergence angle. The laser pulse expels the background plasma electrons to form a plasma bubble with strong quasistatic radial electric and azimuthal magnetic fields. Self-injected electrons trapped in the bubble are betatron accelerated and focused by the latter. The relativistic vortical motion of such helically distributed electrons can generate gamma rays through nonlinear synchrotron radiation. In particular, with a $10^{22}$ W/cm$^2$ LG laser pulse, the peak brightness of the helically distributed 1-MeV gamma rays can reach $2.23 \times 10^{24}$ photons/s/mm$^2$/mrad$^2$/0.1% BW and their emission angle can be reduced to approximately $10^\circ$ by tailoring the focusing fields in the plasma bubble. In addition, it is shown that in present scheme, the OAM of the generated gamma rays increases linearly with the topological charge and intensity of the LG laser.

## II. SIMULATION RESULTS

To demonstrate the proposed scheme, we carry out three-dimensional (3D) particle-in-cell (PIC) simulations using the well-known EPOCH3D code [37], with the QED BLOCK enabled to include the emission of gamma photons via a Monte Carlo algorithm, the radiation reaction effect on electron dynamics, and the feedback between the plasma and photon-emission processes. A CP LG laser pulse with peak intensity $2 \times 10^{22}$ W/cm$^2$ and wavelength $\lambda = 0.8$ $\mu$m is incident from the left boundary of the simulation box of size $100 \times 50 \times 50$ $\mu$m, with $1000 \times 250 \times 250$ grids and four particles per cell. The initial spatial distribution of the laser pulse in cylindrical coordinates $(r, \theta, z$, where $r^2 = y^2 + z^2)$ is $\vec{a} = a_0 C_l^p (\cos\theta \vec{e}_y + \sigma \sin\theta \vec{e}_z)(\sqrt{2}r/r_0)^{|l|} \exp(-r^2/r_0^2) L_l^p \exp(-il\theta)$, where $a_0 = eE_{y0}/m_e\omega_0 c$ is the normalized peak light-wave electric field $E_{y0}$, $e$ is the elementary charge, $\omega_0$ is the central laser frequency, $r_0$ is the spot radius, $l$ is the topological charge, and $p$ is the node number of the input LG pulse, $c$ is the light speed in vacuum, and $\vec{e}_j$ $(j = x, y, z)$ denote the unit vectors. For definitiveness, we set $r_0 = 7$ $\mu$m, $\sigma = +1$ for right-hand CP, and $p = 0$, so that $L_l^p = 1$. The laser-pulse duration and rise time are $\tau = 20T_0$ and $5T_0$, respectively, where $T_0 = \lambda/c$ is the laser cycle. The electron density and the electron and ion temperatures of the uniform background plasma (located in $5 < x[\mu\text{m}] < 100$) are $n_e = 2.4 \times 10^{20}$ cm$^{-3}$ and 1 keV and 30 eV, respectively. The parameters are chosen such that the laser-pulse length $c\tau$ is near the estimated length $[2\lambda\sqrt{a_l n_c/n_e}/\pi$, where $n_c \sim 1.74 \times 10^{21}$ cm$^{-3}$ is the critical density and $a_l = a_0 l^l \exp(-l/2)$ is the laser amplitude] of the resonant plasma bubble that it creates [38,39]. In this regime, both the laser and the quasistatic self-generated charge-separation electric fields play important roles in accelerating the electrons [38]. In the simulations, the time step is set as $\Delta t = 0.01T_0$, which is much smaller than $\Delta t_{\text{qed}}$ so that a particle can emit multiple times over the duration $\Delta t_{\text{qed}}$. In this case, the time setup satisfies the constraint for QED-PIC simulations [37]. In addition, we check that the simulation results are convergent under the present setup conditions.

Figures 1 and 2 show the simulation results at $t = 100T_0$. It is shown from Fig. 1(a) that the electric field of the CP LG laser pulse has a helical intensity profile and is null on the axis. Thus, the ponderomotive force drives the affected electrons in the underdense background plasma radially outward as well as inward, forming an elongated-donut-shape d bubble with compressed plasma on the axis, as shown in Fig. 2(a). For the parameters chosen, the bubble size is comparable with that of the laser pulse and electrons can become trapped in the helical laser fields. These electrons gain energy as well as angular momentum from the CP LG laser [38] and they have a hollow helical distribution, as can be seen in Fig. 2(a). Figure 2(b) is for the focusing field $W_r = E_r - cB_\theta \propto$

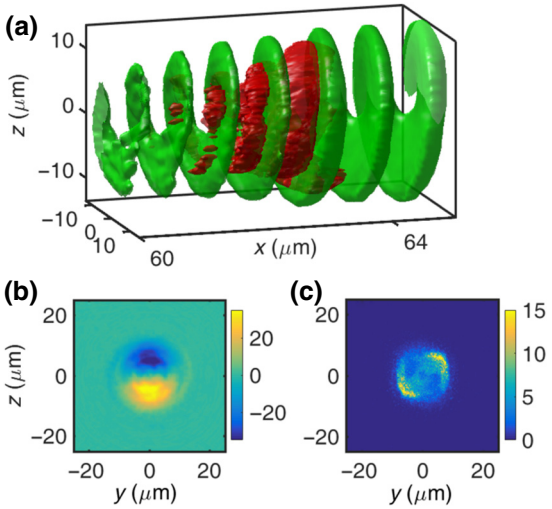


FIG. 1. (a) The isosurfaces of the normalized electric field $eE_y/m_e\omega c$ (green, for isosurface value 7) of the $l = 1$ LG laser light and the normalized energy density $\mathcal{E}_{\text{photon}}/n_c m_e c^2$ (red, for isosurface value 16.5) of the generated gamma photons at $t = 100T_0$ at $x = 61.5$ $\mu$m. The isosurface of the radiating trapped electron is similar to the latter. The transverse ($y$-$z$ plane) distributions of the normalized (b) laser electric field and (c) photon energy density.

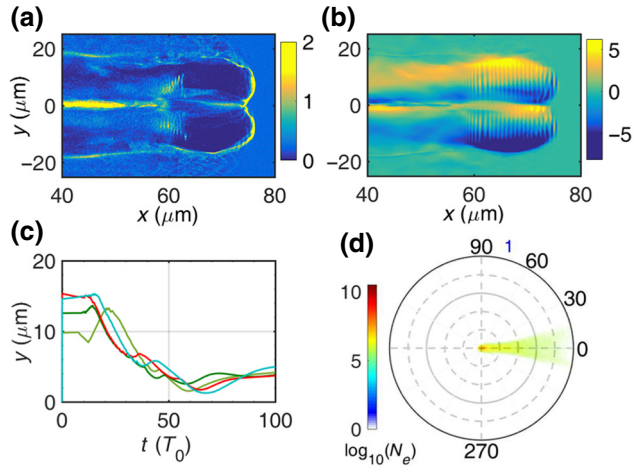


FIG. 2. (a) The transverse ($z = 0$ plane) profile of the electron density normalized by $n_c$ along the laser propagation direction $x$, at $t = 100T_0$. One can see (around $y = 0, x = 60\ \mu$m) the helical betatron-oscillating electron bunches. Since during the process the structure also rotates around the center axis (i.e., $r = 0$), the resulting electron density distribution has a helical structure (not shown), similar to that of the energy density of the photons emitted by these electrons given by the red isosurface in Fig. 1(a). (b) The normalized acceleration field $e(E_r - cB_\theta)/m_e\omega c$. (c) The trajectories of four typical electrons starting from different radial locations. Here, one can clearly see the focusing and collimation effects. (d) The angular distribution of the accelerated electrons in the $x$-$y$ plane. Here, the radius represents the electron energy normalized by its maximum value and the polar angle $\phi = 0$ is in the laser propagation, or $x$, direction. The color code is for the electron number $N_e$.

$a^2(r)r^{-1}[1 - 2(r/r_0)^2]\cos\xi$, where $E_r$ is the radial electric field and $B_\theta$ is the azimuthal magnetic field experienced by the trapped electrons. The zero point (corresponding to maximum laser intensity) of the transverse focusing field is at $r_m \approx r_0/\sqrt{2} = 5\ \mu$m. The high-energy electrons are confined to this region and they execute transverse betatron oscillations under the focusing field, as can be seen in Fig. 2(c) for four typical electron trajectories. Figure 2(d) clearly shows that these electrons are accelerated mainly forward and the divergence angle is less than 10°, which is considerably smaller than the typical $\gtrsim 30°$ angle from the other laser-acceleration schemes [2,19,33,35,36].

In order to clarify the acceleration process of the trapped electrons in the plasma bubble, the motions of some typical electrons are followed. The energy gained by an electron consists of two parts, namely, $W_x = -\int_0^t ev_xE_xdt$ from the longitudinal field and $W_\perp = -\int_0^t e(v_yE_y + v_zE_z)dt$ from the transverse field. Figure 3(a) shows that initially both fields contribute about equally to the electron acceleration and that the energy gain is periodic, as expected since the electrons are overlapped and directly driven by the laser fields. When betatron resonance occurs (say, at $t = 35T_0$), or the betatron frequency gets close to the

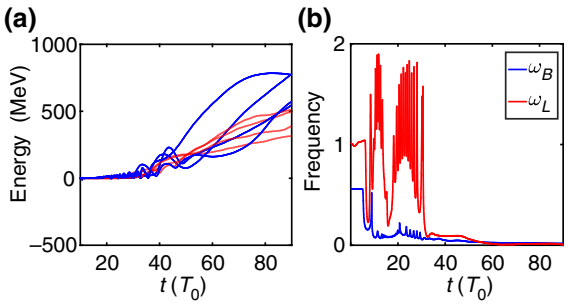


FIG. 3. (a) The evolution of the energy gain of three typical electrons from the longitudinal $W_x = -\int_0^t ev_xE_xdt$ (blue curves) and the transverse $W_\perp = -\int_0^t e(v_yE_y + v_zE_z)dt$ (red curves) fields. (b) The evolution of the normalized (by the laser frequency $\omega_0$) frequencies $\omega_B$ and $\omega_L$ of the electron betatron oscillations and the laser in the electron comoving frame, respectively, as experienced by the electron.

Doppler-shifted laser frequency, the electron can stay in the acceleration phase of the laser field for a long time, so that the energy gain is no longer periodic, as shown in Fig. 3(a). The betatron resonance behavior is also confirmed in Fig. 3(b) for the evolution of the betatron and laser frequencies as witnessed by an accelerated electron. This scenario of electron energy gain can end if the electron becomes detrapped and leaves the accelerating phase of the laser light. Transverse dephasing is mainly due to electron slippage in the acceleration phase of the LG laser fields, which takes place when the electron energy increases such that the resonance condition $\omega_B = (1 - \delta)\omega_L$ is no longer satisfied [22]. Here, $\omega_B$ is the betatron frequency of electrons in the bubble, $\omega_L = (1 - v_x/v_{\rm ph})\omega_0$ is the laser frequency in the electron comoving frame, $v_{\rm ph} = c/\sqrt{1 - \omega_p^2/\gamma\omega_0^2} \approx c(1 + n/2\gamma)$ is the phase velocity of the laser in the bubble, $\gamma = \sqrt{1 + a_l^2} \approx a_l$ is the Lorentz factor, $n = n_e/n_c$, and $\delta \propto d\gamma/\gamma dt$ refers to the frequency shift. The dephasing rate is then $d_t\Phi = \omega_B - \omega_L$ and the dephasing length is $L_{\rm dp} = cT_{\rm dp} = c\pi/|d_t\Phi| = ca_lT_0/2|\delta|n$. On the other hand, longitudinal dephasing of a trapped electron is mainly due to it leaving the acceleration phase in the rear part of the plasma bubble. The corresponding dephasing length is $L_{\rm dp2} = cL/2(c - v_g)$, where $v_g = c\sqrt{1 - \omega_p^2/\gamma\omega_0^2} \approx c(1 - n/2\gamma)$ is the laser group velocity and $L \approx 2\lambda/\pi\sqrt{S} \approx c\tau$ is the longitudinal dimension of the bubble, with $S = n_e/a_ln_c$ being the self-similar parameter. The longitudinal dephasing length is then $L_{\rm dp2} = La_l/n$. Note that for the parameters given here, both the transverse and longitudinal dephasing lengths are larger than 100 $\mu$m and are in good agreement with the simulation results in Fig. 3(a).

Figure 4(a) for the electron energy spectrum shows that the electrons in the bubble can be accelerated to the

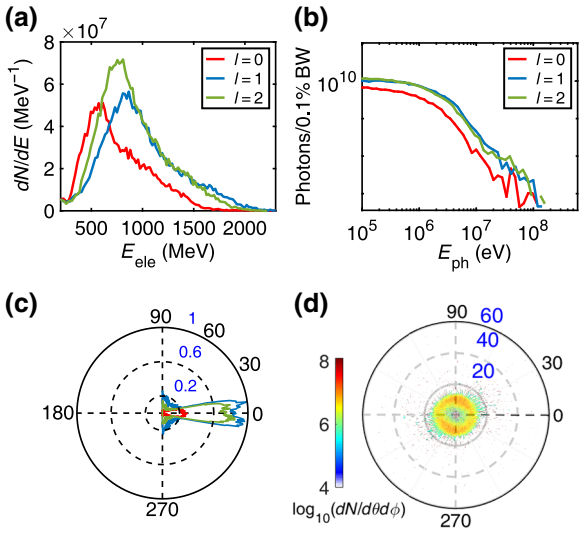


FIG. 4. (a) The energy spectra of the helical electron beam for laser topological charges $l = 0$ (no OAM, red curve), $l = 1$ (blue curve), and $l = 2$ (green curve) in the plasma bubble at $100T_0$. (b) The energy spectra of the gamma photons for 0.1% bandwidth. In all cases, the slope of the high-energy part is approximately $-0.71$, in agreement with that of typical synchrotron radiation. The critical energy is around $E_{\rm ph} = 2 \times 10^5$ eV (note that we have not tracked the lower-energy photons). (c) The energy distribution in the $x$-$y$ plane of the gamma photons for $l = 0, 1$, and 2 [same color code as in (a)]. Here, the polar angle is given by $\phi = \arctan(p_y/p_x)$ and the radius represents the photon energy normalized by the maximum value, which is from the laser with $l = 1$. Recall that the laser propagates in the $x$, or $\phi = 0$, direction. (d) The $y$-$z$, or transverse, plane energy distribution (given by the color bar) of energetic ($\mathcal{E} \geq 1$ MeV) gamma photons for $l = 1$. Here, the polar angle is $\Psi = \arctan(p_y/p_z)$ and the radial coordinate is for the $x$-$y$-plane polar angle, e.g., 20°, 40°, and 60°.

giga-electron-volt level, as they can stay in the acceleration phase for a long time. Correspondingly, a vortex gamma-ray pulse with energy density $> 16.5 n_c m_e c^2$ and duration 12 fs is generated. The maximum radiation energy is about 5.6 J. The maximum photon energy exceeds 100 MeV and the photon number in a 0.1% bandwidth (BW) around 1 MeV is about $10^{10}$ for $l \neq 0$. In particular, for $l = 2$, the peak brightness of the gamma-ray pulse at 1 MeV is about $2.23 \times 10^{24}$ photons/s/mm$^2$/mrad$^2$/0.1% BW, which is about 2 orders of magnitude higher than the record achieved by inverse Compton scattering based on laser-wake-field acceleration scheme [40]. It is noted that the maximum electron energy and gamma photon energy are similar in these cases; however, more high-energy electrons and more gamma photons can be generated if $l$ is suitably chosen, as can be seen in Figs. 4(a) and 4(b), because the laser topological charge $l$ determines the number of phases for electron acceleration [38]. Thus in cases with $l \neq 0$, more electrons can be accelerated and more photons can be emitted compared with $l = 0$. It is shown that the photon spectra here are similar to those of typical synchrotron radiation. It is known that synchrotron-radiation photons are emitted nearly parallel to the velocity of the relativistic electrons; thus the photons are highly localized and collimated to within an angle $\phi \leq 10°$, as can be seen in Figs. 4(c) and 4(d) for the distribution of the gamma-ray energy.

In order to calculate the OAM of an accelerated electron beam and an emitted photon beam, one can start with the equations of momentum $\vec{p}$ and energy $\gamma$ evolution for a typical electron in the bubble, as follows:

$$\frac{d\vec{p}}{dt} = -e\left[\vec{E}_L + \frac{\vec{v}}{c} \times \left(\vec{B}_L + \vec{B}_{S\theta} + \vec{B}_{Sx}\right)\right], \quad (1)$$

$$m_e c^2 \frac{d\gamma}{dt} = -e\vec{v} \cdot \vec{E}_L, \quad (2)$$

where $\vec{E}_L = E_{Ly}\vec{y} + E_{Lz}\vec{z}$, $\vec{B}_L = B_{Ly}\vec{y} + B_{Lz}\vec{z}$, and the subscripts $L$ and $S$ denote laser and self-generated quantities, respectively. The transverse motion of the electron is then given by the following:

$$\frac{dp_y}{dt} = -e\kappa E_L \cos\Phi + ev_x B_{Sz} - ev_z B_{Sx}, \quad (3)$$

$$\frac{dp_z}{dt} = -e\kappa E_L \sin\Phi - ev_x B_{Sy} + ev_y B_{Sx}, \quad (4)$$

where $\kappa = 1 - v_x/v_{\rm ph}$. Equations (3) and (4) can be solved by noting that the motion in the laser oscillating fields is much faster than that driven by the ponderomotive force and self-fields. Accounting for the condition $\omega_B \approx \omega_L$ for betatron resonance, the transverse momentum of a betatron electron is then given by $p_y(t) = -m_e c a_l(\omega_L t/2)\cos\theta$ and $p_z(t) = m_e c a_l(\omega_L t/2)\sin\theta$. Thus, the trajectory in the transverse plane is given by $y(t) = \int[p_y(t)/\gamma m_e]dt$ and $z(t) = \int[p_z(t)/\gamma m_e]dt$. The angular momentum of the electron beam with respect to the $x$ axis can be written as follows:

$$L_x = \sum_i [\vec{r}_i \times \vec{p}_i]_x = \sum_i [yp_{i,z} - zp_{i,y}]_x. \quad (5)$$

The number of resonance electrons ($N_e$) can be estimated by $N_e \approx n_e \pi R^2 c\tau \approx a_l n_c \lambda^2 c\tau/\pi$ [22], where $R = \lambda/\pi\sqrt{S}$ is the self-focused laser spot radius, $\tau$ is the duration of the laser pulse, and $\lambda$ is the laser wavelength. The angular momentum of the LG laser pulse is [41] $L_{\rm laser} \approx -(l+\sigma)I_0\pi r_0^2\tau/2\omega_0$, where $l$ and $\sigma$ are related to the laser orbital and spin angular momenta, respectively, and $I_0 = m_e c^3 n_c a_l^3$ is the peak laser intensity. The angular momentum transferred from the LG laser pulse to the electrons has been derived in Ref. [42]. In view of Eq. (5), we can write

the following:

$$L_{\rm ele} \simeq -(l+\sigma)C_1 S^{1/2} m_e c^2 a_l^2 t_a n_c \lambda^2 c\tau, \qquad (6)$$

where $C_1$ is a constant and $t_a$ is the electron acceleration time in the LG laser pulses [42].

The relativistic spiraling electrons emit synchrotron radiation. In the process, their angular momentum is in turn transferred to the emitted photons, so that a train of gamma photons with OAM is generated, as can be seen in Figs. 1(a) and 5(a)–5(c). The former indicates that the energy density of the gamma photons has a quasiperiodic vortex distribution that rotates around the laser axis. Transverse sectional views of the gamma-photon energy density are shown in Figs. 5(a)–5(c). Since not all the angular momentum of the electron bunch is transferred to the gamma photons, we can write for the angular momentum of the latter along the axis,

$$L_x = C_2 L_{\rm ele}, \qquad (7)$$

where $C_2$ is a constant that represents the transfer efficiency. An equivalent expression has been obtained in Ref. [43], which considered in detail the radiation from a given spiraling electron. Figure 5(d) shows the evolution of the photon angular momentum for the laser topological charges $l = 0, 1$, and 2 and we can see that the photon angular momentum (normalized by $\lambda m_e c = 2.18 \times 10^{-28}$ kg m$^2$/s) can reach $-1.20 \times 10^{13}$, $-2.14 \times 10^{13}$, and $-3.25 \times 10^{13}$, respectively. Figure 5(e) shows that with the same input laser energy, the angular momentum of the gamma photons depends linearly on the laser topological charge $l + \sigma$, in agreement with the above analysis. Correspondingly, the laser-to-photon angular-momentum conversion rates are almost the same (about 2.0%, 1.83%, and 1.86%, respectively) in these cases, and the laser-to-photon energy- (above 100 keV) conversion rates are 0.39%, 0.95%, and 1.1%, respectively, and roughly depend linearly on the value of $l + \sigma$, which in turn governs the number of gamma-photon bunches.

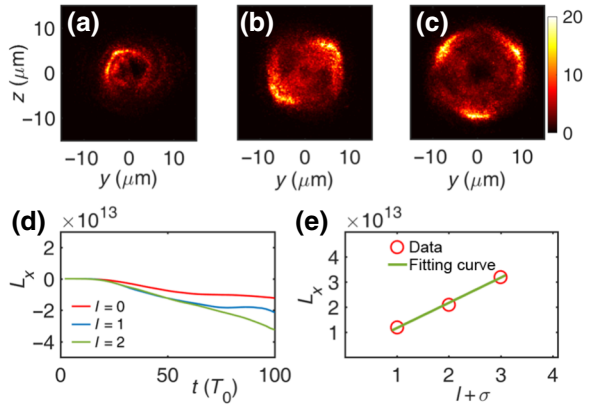


FIG. 5. (a)–(c) The $y$-$z$ cross-section view of the photon energy densities (in units of $n_c m_e c^2$) at $x = 61.5$ $\mu$m for $\sigma = 1$ and $l = 0, 1$, and 2, respectively. (d) The evolution of the angular momentum of the gamma photons for $l = 0, 1$, and 2. (e) The dependence of the angular momentum of the gamma photons on the topological charge. The green curve is a linear fit.

## III. DISCUSSION

It should be noted that at present, the maximum intensity of LG laser light achieved experimentally is about $10^{20}$ W/cm$^2$, namely from the petawatt-class laser facility PHELIX at the Gesellschaft für Schwerionenforschung (GSI), in Germany. This intensity is still below the effective range needed for the operation of the proposed scheme. However, novel techniques for generating more intense LG laser light, such as the use of multilevel spiral phase plates [44], plasma holograms [45], Raman amplification [46], light fans [47], chirped pulse amplification of weaker LG light [48], etc. are at present being actively investigated. Hopefully, LG laser pulses of higher intensity will soon become available.

To demonstrate the effect of laser intensity on the generation of gamma photons, we conduct a series of simulations with different laser amplitudes but the same topological charge $l = 2$. Figure 6 shows that the dependence of the electron and photon angular momenta on the laser amplitude $a_0$ approximately follows an $a_0^2$ scaling, which agrees well with the theoretical analysis [Eqs. (6) and (7)] in Sec. II. Under conditions with lower laser intensities, the mechanisms of electron acceleration and radiation still work efficiently as long as the self-similar parameter $S$ is fixed; however, the angular momenta and the number of emitted photons decrease as the laser amplitude decreases. In particular, with the presently available laser intensities, such as $5.5 \times 10^{20}$ W/cm$^2$, the angular momentum of the gamma photons can still reach $4.32 \times 10^{-16}$ kg m$^2$/s, and the corresponding torque of the gamma rays can still be 3 orders of magnitude higher than that generated in existing experiments [49], an improvement that can be useful in many applications.

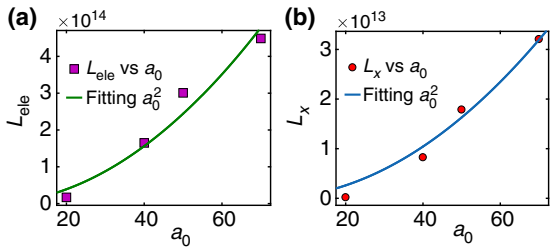


FIG. 6. The dependence of the (a) electron and (b) photon angular momentum on the laser amplitude $a_0$ at $100T_0$ for $l = 2$ with the same self-similar parameter $S = n_e/a_l n_c$. The angular momenta of the electrons and photons are normalized by $\lambda m_e c = 2.18 \times 10^{-28}$ kg m$^2$/s.

## IV. SUMMARY

In summary, we propose a scheme for generating gamma rays with a high level of brilliance, a low divergence angle, and controllable angular momentum. In this scheme, bright gamma rays are realized from synchrotron radiation of the helical energetic electron bunch accelerated and collimated by the LG laser and the favorably structured self-generated quasistatic fields in the plasma bubble. The resulting gamma rays obtain angular momentum from the spiraling relativistic electrons and thus also have a vortical structure, as can be seen in Fig. 1(a). The gamma-ray OAM can be controlled by varying the topological charge and power of the incident laser pulse. Such intense gamma rays with controllable OAM offer an additional degree of freedom as well as unique characteristics, which can be useful in a wide range of applications—including quantum-electrodynamic effects, laboratory astrophysics, high-flux positron generation, the probing of magnetism in materials, etc.—that involve vortical structure and motion.

## ACKNOWLEDGMENTS

This work is supported by the National Key R&D Program of China (Grant No. 2016YFA0401100), the National Natural Science Foundation of China (Grants No. 11575031 and No. 11705120), the Featured Innovation Project of the Educational Commission of Guangdong Province of China (Grant No. 2018KTSCX352), and the Natural Science Foundation of Top Talent of SZTU (Grant No. 2019010801001). The EPOCH code is used under the United Kingdom Engineering and Physical Sciences Research Council (EPSRC) Contract (EP/G055165/1 and EP/G056803/1).

L. B. Ju and T. W. Huang contributed equally to this work.

[1] Y. V. Lun, C. W. Wong, K. H. Lai, and T. Cheng, Institutional perspective on the adoption of technology for the security enhancement of container transport, Transport Rev. **28**, 21 (2008).

[2] C. P. Ridgers, C. S. Brady, R. Duclous, J. G. Kirk, K. Bennett, T. D. Arber, A. P. L. Robinson, and A. R. Bell, Dense Electron-Positron Plasmas and Ultraintense $\gamma$-Rays from Laser-Irradiated Solids, Phys. Rev. Lett. **108**, 165006 (2012).

[3] H. X. Chang, B. Qiao, Z. Xu, X. R. Xu, C. T. Zhou, X. Q. Yan, S. Z. Wu, M. Borghesi, M. Zepf, and X. T. He, Generation of overdense and high-energy electron-positron-pair plasmas by irradiation of a thin foil with two ultraintense lasers, Phys. Rev. E **92**, 053107 (2015).

[4] Y. Eisen, A. Shor, and T. Mardor, CdTe and CdZnTe gamma ray detectors for medical and industrial imaging systems, Nucl. Instrum. Methods Phys. Res. A **428**, 158 (1999).

[5] J. Ganz, *Gamma Knife Neurosurgery* (Springer-Verlag, Wien, 2011).

[6] R. W. Schoenlein, W. P. Leemans, A. H. Chin, P. Volfbeyn, T. E. Glover, P. Balling, M. Zolotorev, K.-J. Kim, S. Chattopadhyay, and C. V. Shank, Femtosecond X-ray pulses at 0.4 Å generated by 90 Thomson scattering: A tool for probing the structural dynamics of materials, Science **274**, 236 (1996).

[7] A. Giulietti *et al.*, Intense $\gamma$-Ray Source in the Giant-Dipole-Resonance Range Driven by 10-TW Laser Pulses, Phys. Rev. Lett. **101**, 105002 (2008).

[8] J. Galy, M. Maučec, D. J. Hamilton, R. Edwards, and J. Magill, Bremsstrahlung production with high-intensity laser matter interactions and applications, New J. Phys. **9**, 23 (2007).

[9] K. W. D. Ledingham and W. Galster, Laser-driven particle and photon beams and some applications, New J. Phys. **12**, 045005 (2010).

[10] K. Ta Phuoc, S. Corde, C. Thaury, V. Malka, A. Tafzi, J. P. Goddet, R. C. Shah, S. Sebban, and A. Rousse, All-optical Compton gamma-ray source, Nat. Photonics **6**, 308 (2012).

[11] N. D. Powers, I. Ghebregziabher, G. Golovin, C. Liu, S. Chen, S. Banerjee, J. Zhang, and D. P. Umstadter, Quasi-monoenergetic and tunable X-rays from a laser-driven Compton light source, Nat. Photonics **8**, 28 (2014).

[12] G. Sarri *et al.*, Generation of neutral and high-density electron positron pair plasmas in the laboratory, Nat. Commun. **6**, 6747 (2015).

[13] Z. Gong, R. H. Hu, H. Y. Lu, J. Q. Yu, D. H. Wang, E. G. Fu, C. E. Chen, X. T. He, and X. Q. Yan, Brilliant GeV gamma-ray flash from inverse Compton scattering in the QED regime, Plasma Phys. Control. Fusion **60**, 044004 (2018).

[14] T. W. Huang, C. M. Kim, C. T. Zhou, C. M. Ryu, K. Nakajima, S. C. Ruan, and C. H. Nam, Tabletop laser-driven gamma-ray source with nanostructured double-layer target, Plasma Phys. Control. Fusion **60**, 115006 (2018).

[15] T. W. Huang, C. M. Kim, C. T. Zhou, M. H. Cho, K. Nakajima, C. M. Ryu, S. C. Ruan, and C. H. Nam, Highly efficient laser-driven Compton gamma-ray source, New J. Phys. **21**, 013008 (2019).

[16] J. Ferri, S. Corde, A. Döpp, A. Lifschitz, A. Doche, C. Thaury, K. Ta Phuoc, B. Mahieu, I. A. Andriyash, V. Malka, and X. Davoine, High-Brilliance Betatron $\gamma$-Ray Source Powered by Laser-Accelerated Electrons, Phys. Rev. Lett. **120**, 254802 (2018).

[17] S. Corde and K. Ta Phuoc, Plasma wave undulator for laser-accelerated electrons, Phys. Plasmas **18**, 033111 (2011).

[18] H. X. Chang, B. Qiao, T. W. Huang, Z. Xu, C. T. Zhou, Y. Q. Gu, X. Q. Yan, M. Zepf, and X. T. He, Brilliant petawatt gamma-ray pulse generation in quantum electrodynamic laser-plasma interaction, Sci. Rep. **7**, 45031 (2017).

[19] C. S. Brady, C. P. Ridgers, T. D. Arber, A. R. Bell, and J. G. Kirk, Laser Absorption in Relativistically Underdense Plasmas by Synchrotron Radiation, Phys. Rev. Lett. **109**, 245006 (2012).

[20] T. W. Huang, C. T. Zhou, H. Zhang, S. Z. Wu, B. Qiao, X. T. He, and S. C. Ruan, Collimated gamma photon emission

driven by PW laser pulse in a plasma density channel, Appl. Phys. Lett. **110**, 021102 (2017).

[21] X. L. Zhu, Y. Yin, T. P. Yu, F. Q. Shao, Z. Y. Ge, W. Q. Wang, and J. J. Liu, Enhanced electron trapping and $\gamma$ ray emission by ultra-intense laser irradiating a near-critical-density plasma filled gold cone, New J. Phys. **17**, 053039 (2015).

[22] T. W. Huang, A. P. L. Robinson, C. T. Zhou, B. Qiao, B. Liu, S. C. Ruan, X. T. He, and P. A. Norreys, Characteristics of betatron radiation from direct-laser-accelerated electrons, Phys. Rev. E **93**, 063203 (2016).

[23] A. V. Arefiev, B. N. Breizman, M. Schollmeier, and V. N. Khudik, Phys. Rev. Lett. 108, 145004 (2012); A. V. Arefiev, V. N. Khudik, and M. Schollmeier, Enhancement of laser-driven electron acceleration in an ion channel, Phys. Plasmas 21, 033104 (2014).

[24] S. Corde, K. Ta Phuoc, G. Lambert, R. Fitour, V. Malka, A. Rousse, A. Beck, and E. Lefebvre, Femtosecond X-rays from laser-plasma accelerators, Rev. Mod. Phys. **85**, 1 (2013).

[25] J. S. Liu, C. Q. Xia, W. T. Wang, H. Y. Lu, Ch. Wang, A. H. Deng, W. T. Li, H. Zhang, X. Y. Liang, Y. X. Leng, X. M. Lu, C. Wang, J. Z. Wang, K. Nakajima, R. X. Li, and Z. Z. Xu, All-Optical Cascaded Laser Wakefield Accelerator Using Ionization-Induced Injection, Phys. Rev. Lett. **107**, 035001 (2011).

[26] W. T. Wang, W. T. Li, J. S. Liu, Z. J. Zhang, R. Qi, C. H. Yu, J. Q. Liu, M. Fang, Z. Y. Qin, C. Wang, Y. Xu, F. X. Wu, Y. X. Leng, R. X. Li, and Z. Z. Xu, High-Brightness High-Energy Electron Beams from a Laser Wakefield Accelerator via Energy Chirp Control, Phys. Rev. Lett. **117**, 124801 (2016).

[27] M. Martinez, in *Boulder Damage Symposium XXXVII: Annual Symposium on Optical Materials for High Power Lasers* (SPIE—International Society for Optical Engineering, Bellingham, 2005).

[28] The extreme light infrastructure: http://www.eli-laser.eu.

[29] M. Padgett and R. Bowman, Tweezers with a twist, Nat. Photonics **5**, 343 (2011).

[30] J. Wang, J. Y. Yang, I. M. Fazal, N. Ahmed, Y. Yan, H. Huang, Y. X. Ren, Y. Yue, S. Dolinar, M. Tur, and A. E. Willner, Terabit free-space data transmission employing orbital angular momentum multiplexing, Nat. Photonics **6**, 488 (2012).

[31] G. Molina-Terriza, J. P. Torres, and L. Torner, Twisted photons, Nat. Phys. **3**, 305 (2007).

[32] F. Tamburini, B. Thidé, and G. Molina, Twisting of light around rotating black holes, Nat. Phys. **7**, 195 (2011).

[33] C. Liu, B. F. Shen, X. M. Zhang, Y. Shi, L. L. Ji, W. P. Wang, L. Q. Yi, L. G. Zhang, T. J. Xu, Z. K. Pei, and Z. Z. Xu, Generation of gamma-ray beam with orbital angular momentum in the QED regime, Phys. Plasmas **23**, 093120 (2016).

[34] Y. Y. Chen, J. X. Li, K. Z. Hatsagortsyan, and C. H. Keitel, $\gamma$-Ray Beams with Large Orbital Angular Momentum via Nonlinear Compton Scattering with Radiation Reaction, Phys. Rev. Lett. **121**, 074801 (2018).

[35] R. Capdessus, E. d'Humières, and V. T. Tikhonchuk, Influence of ion Mass on Laser-Energy Absorption and Synchrotron Radiation at Ultrahigh Laser Intensities, Phys. Rev. Lett. **110**, 215003 (2013).

[36] T. Nakamura, J. K. Koga, T. Z. Esirkepov, M. Kando, G. Korn, and S. V. Bulanov, High-Power $\gamma$-Ray Flash Generation in Ultraintense Laser-Plasma Interactions, Phys. Rev. Lett. **108**, 195001 (2012).

[37] T. D. Arber, K. Bennett, C. S. Brady, A. Lawrence-Douglas, M. G. Ramsay, N. J. Sircombe, P. Gillies, R. G. Evans, H. Schmitz, A. R. Bell, and C. P. Ridgers, Contemporary particle-in-cell approach to laser-plasma modelling, Plasma Phys. Control. Fusion **57**, 113001 (2015).

[38] L. B. Ju, C. T. Zhou, K. Jiang, T. W. Huang, H. Zhang, T. X. Cai, J. M. Cao, B. Qiao, and S. C. Ruan, Manipulating the topological structure of ultrarelativistic electron beams using Laguerre Gaussian laser pulse, New J. Phys. **20**, 063004 (2018).

[39] J. L. Shaw, N. Lemos, L. D. Amorim, N. Vafaei-Najafabadi, K. A. Marsh, F. S. Tsung, W. B. Mori, and C. Joshi, Role of Direct Laser Acceleration of Electrons in a Laser Wakefield Accelerator with Ionization Injection, Phys. Rev. Lett. **118**, 064801 (2017).

[40] C. H. Yu *et al.*, Ultrahigh brilliance quasi-monochromatic MeV $\gamma$-rays based on self-synchronized all-optical Compton scattering, Sci. Rep. **6**, 29518 (2016).

[41] L. Allen, M. W. Beijersbergen, R. J. C. Spreeuw, and J. P. Woerdman, Orbital angular momentum of light and the transformation of Laguerre-Gaussian laser modes, Phys. Rev. A **45**, 8185 (1992).

[42] L. B. Ju, C. T. Zhou, T. W. Huang, K. Jiang, H. Zhang, S. Z. Wu, B. Qiao, and S. C. Ruan, Production of high-angular-momentum electron beams in laser-plasma interactions, Phys. Rev. E **95**, 053205 (2017).

[43] M. Katoh, M. Fujimoto, H. Kawaguchi, K. Tsuchiya, K. Ohmi, T. Kaneyasu, Y. Taira, M. Hosaka, A. Mochihashi, and Y. Takashima, Angular Momentum of Twisted Radiation from an Electron in Spiral Motion, Phys. Rev. Lett. **118**, 094801 (2017).

[44] K. Sueda, G. Miyaji, N. Miyanaga, and M. Nakatsuka, Laguerre-Gaussian beam generated with a multilevel spiral phase plate for high intensity laser pulses, Opt. Express **12**, 3548 (2004).

[45] A. Leblanc, A. Denoeud, L. Chopineau, G. Mennerat, Ph. Martin, and F. Quèrè, Plasma holograms for ultrahigh-intensity optics, Nat. Phys. **13**, 440 (2017).

[46] J. Vieira, R. M. G. M. Trines, E. P. Alves, R. A. Fonseca, J. T. Mendonça, R. Bingham, P. A. Norreys, and L. O. Silva, Amplification and generation of ultra-intense twisted laser pulses via stimulated Raman scattering, Nat. Commun. **7**, 10371 (2016).

[47] Y. Shi, B. F. Shen, L. G. Zhang, X. M. Zhang, W. P. Wang, and Z. Z. Xu, Light Fan Driven by a Relativistic Laser Pulse, Phys. Rev. Lett. **112**, 235001 (2014).

[48] C. Brabetz, S. Busold, T. Cowan, O. Deppert, D. Jahn, O. Kester, M. Roth, D. Schumacher, and V. Bagnoud, Laser-driven ion acceleration with hollow laser beams, Phys. Plasmas **22**, 013105 (2015).

[49] M. Zurch, C. Kern, P. Hansinger, A. Dreischuh, and C. Spielmann, Strong-field physics with singular light beams, Nat. Phys. **8**, 743 (2012).